JOC
The Journal of Organic Chemistry

Article

Pyrido[1,2-e]purine: Design and Synthesis of Appropriate Inhibitory Candidates against the Main Protease of COVID-19

Parvin Moghimi, Hossein Sabet-Sarvestani, Omid Kohandel, and Ali Shiri*

Cite This: https://doi.org/10.1021/acs.joc.1c02237

Read Online

ACCESS | 📊 Metrics & More | 📖 Article Recommendations | SI Supporting Information

ABSTRACT: A series of tricyclic and polycyclic pyrido[1,2-e]purine derivatives were designed and synthesized via a two-step, one-pot reaction of 2,4-dichloro-5-amino-6-methylpyrimidine with pyridine under reflux conditions. Various derivatives of pyrido[1,2-e]purine were also synthesized by substituting the chlorine atom with secondary amines. After careful physiochemical and pharmacokinetic predictions, the inhibitory effects of the synthesized compounds against the main protease of SARS-CoV-2 have been evaluated by molecular docking and molecular dynamics approaches. The in silico results revealed that among all of the studied compounds, the morpholine/piperidine-substituted pyrido[1,2-e]purine derivatives are the best candidates as effective inhibitors of SARS-CoV-2.

One-pot 2 steps | X-Ray | Derivatives | Molecular Docking Molecular Dynamics

Inhibitory Candidates Against the Main Protease of COVID-19
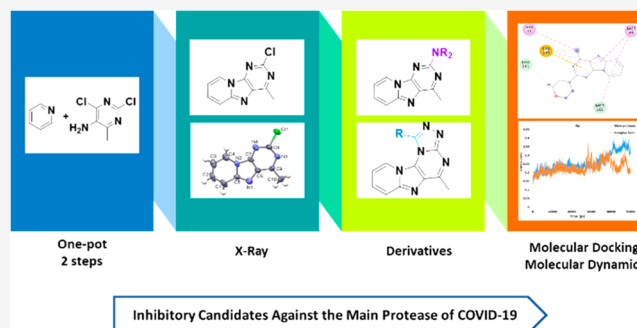
INTRODUCTION

SARS-CoV-2, a single-stranded positive RNA, is a newly recognized member of the coronavirus family that causes a pandemic (COVID-19) infectious disease that is a serious global health and economic threat.[1,2] The genomic sequence of SARS-CoV-2 is 79% similar with the SARS-CoV genome.[3,4] The main protease of SARS-CoV-2, the chymotrypsin-like cysteine protease (3CL^{pro}), is composed of two identical polypeptides and contains 300 amino acid residues. This enzyme plays a vital role in virus replication. In structural analysis, the 3CL^{pro} enzyme consists of three domains: domain I (residues 8−101), domain II (residues 102−184), and domain III (residues 201−303). The chymotrypsin structure formed by the first two domains is known as a β-barrel, and the third domain consists of five α-helices. The active site of 3CL^{pro}, located between domains I and II, includes Cys145 and His41 amino acid residues. These amino acids form a catalytic dyad that is responsible for viral genome replication.[5−7] Therefore, two separate diverse potent inhibitors of 3CL^{pro}, including both peptidomimetic inhibitors and nonpeptidic inhibitors, have been reported to overcome the rapid spread of the COVID-19 pandemic.[8−12]

Recently, studies have illustrated that N-heterocyclic compounds possess antiviral activity. Thus, they can be used as potential noncovalent inhibitors of 3CL^{pro} of SARS-CoV-2.[13−16] Some of the most prominent nitrogen-containing heterocycles are the purine scaffolds, which have attracted medicinal interest due to their applications as drug candidates in cancer treatment and viral disorders.[17,18] Also, there is a considerable tendency to study new heterocyclic fused imidazopyridine derivatives containing abundant biological activities, such as anticancer,[19,20] antiprotozoal agent,[21]

antiviral,[22] anti-inflammatory,[23] and anti-Alzheimer's disease[24] activities. Recent investigations have revealed that the heterocyclic systems with additional fused rings display more effective pharmacological and physicochemical properties. Thus, purine-fused tricyclic and polycyclic derivatives have been classified as practical frameworks.[25−27] Moreover, pyrido-[1,2-e]purine derivatives have important biological activities such as selective inhibitory activity toward phosphodiesterase 5 (PDE5) (I),[28−30] anticancer activity (II and III),[31] and antitumor activity (IV)[32] (Figure 1).

With regard to the significant properties of pyrido[1,2-e]purine, developing novel strategies for synthesizing different skeletons of these systems has attracted significant attention. It has been demonstrated in some classical methods that the functionalized imidazo[1,2-a]pyridine system can be employed as a practical substance in combination with various reagents to afford pyrido[1,2-e]purine scaffolds.[33,34] The other synthetic routes using purine as the precursor include ring-closing metathesis followed by oxidation of 8,9-diallylpurines,[35] copper-catalyzed one-pot sequential allylic amination/cyclo-isomerization of the Boc-protected purine,[36] sequential Suzuki coupling of 9-(2-bromophenyl)purines with 2-bromophenyl-boronic acid followed by intramolecular C−H arylation,[37] and
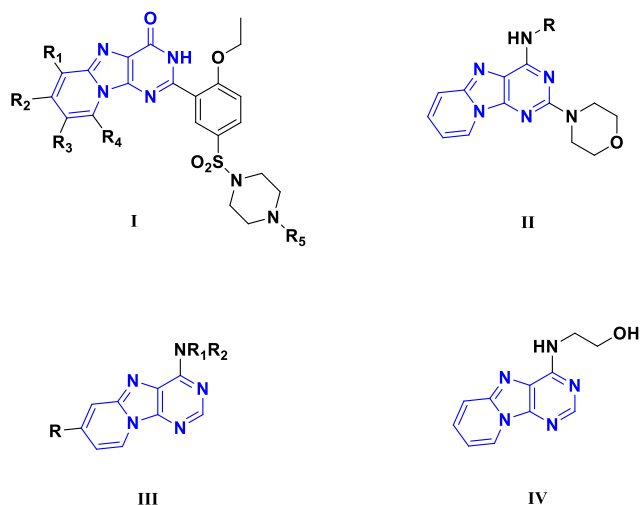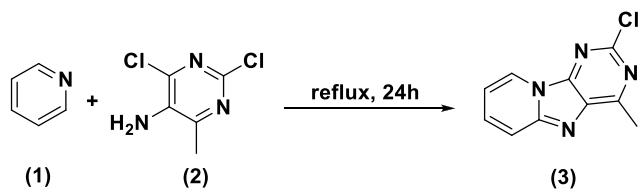
Figure 1. Examples of pyrido[1,2-*e*]purine skeletons possessing biological activities.

Figure 2. Molecular and crystal structure of 2-chloro-4-methylpyrido-[1,2-*e*]purine.

intramolecular cyclization reactions of 1,3-bis(4-methoxybenzyl)-5-(pyridin-2-ylamino)pyrimidine-2,4(1*H*,3*H*)-diones.[38] These methods have shown multistep reactions in the construction of pyrido[1,2-*e*]purine structures. As a continuation of our previous studies,[39−43] herein, we report a two-step, one-pot synthesis of pyrido[1,2-*e*]purine derivatives, and considering the physicochemical and pharmacokinetic predictions, their inhibitory activity against SARS-CoV-2 3CL^{pro} is evaluated using molecular docking and molecular dynamics approaches.

■ RESULTS AND DISCUSSION

In the beginning, 2,4-dichloro-5-amino-6-methylpyrimidine (**2**) was synthesized, according to our previous published procedure.[44] 2,4-Dichloro-5-amino-6-methylpyrimidine (**2**) can react with pyridine used as both a solvent and a substrate under the reflux conditions to generate 2-chloro-4-methylpyrido[1,2-*e*]purine (**3**) (Scheme 1).

Scheme 1. Construction of 2-Chloro-4-methylpyrido[1,2-*e*]purine

Although numerous synthetic methods have been developed to construct the C−N bonds, there is still great demand for milder and cheaper methodologies. The S_NAr and C−H aminations are examples of general approaches implemented to form the C−N bonds of aromatic compounds.[45−47]

Significantly, few reports are recorded to construct pyridopurine skeletons from unsubstituted pyridines in one step,[48,49] and most similar structures have exploited at least two steps to obtain the desired products. Figure 2 depicts the single-crystal X-ray diffraction analysis of the structure of **3**. Crystallographic data for the structure reported here have
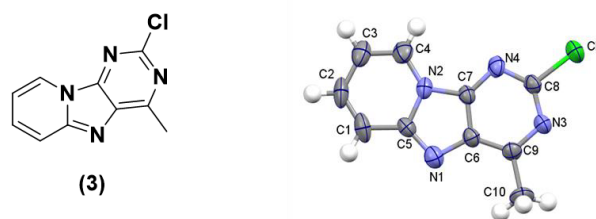
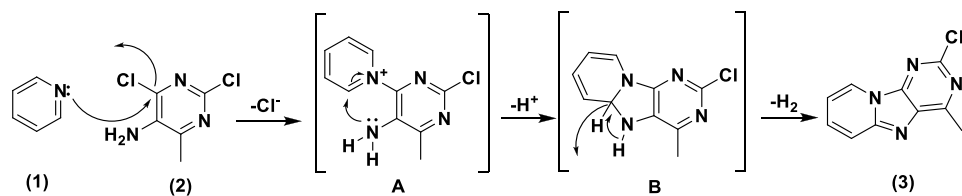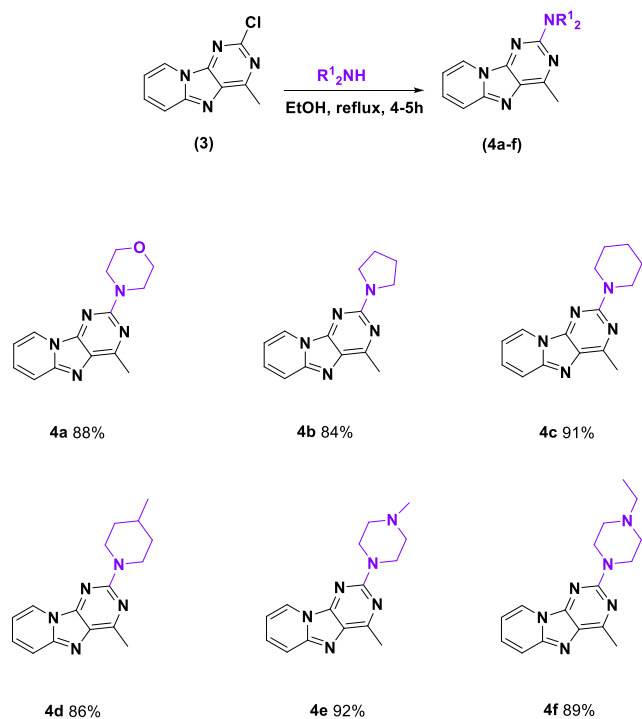been deposited with the Cambridge Crystallographic Data Center (CCDC 2109260).

On the basis of the results, the proposed mechanism has been suggested as a two-step, one-pot pathway, including the formation of a C(sp^2)−N bond through the S_NAr amination of 2,4-dichloro-5-amino-6-methylpyrimidine (**2**) with pyridine followed by direct intramolecular C−H amination. First, the chlorine atom at the C-4 position of compound **2** is replaced with the pyridine ring nitrogen as the nucleophile to afford pyridinium product **A**. Then, the amino group of intermediate **A** attacks the C_α atom of pyridinium, which acts as a highly electrophilic center to furnish intermediate **B**. Finally, removing the hydrogen in the presence of pyridine leads to the corresponding tricyclic structure of **3**.[50,51] The driving force of this phenomenon is the aromatization of the resulting fused tricyclic ring. A plausible reaction mechanism for the synthesis of pyrido[1,2-*e*]purine is depicted in Scheme 2.

In compound **3**, the chlorine atom at the C-2 position can be directly replaced with various secondary amines in ethanol under reflux conditions through the S_NAr reaction to afford the corresponding products (**4a−f**) in 84−92% yields (Table 1).

The treatment of compound **3** with hydrazine hydrate in ethanol under reflux conditions gave 2-hydrazinyl-4-methylpyrido[1,2-*e*]purine (**5**) in 68% yield. Also, the reaction of compound **5** with triethylorthoesters was carried out in various solvents such as ethanol, acetonitrile, chloroform, and acetic acid under reflux conditions to test the effects of the solvents. The results revealed that the reaction in acetic acid has a shorter reaction time and better yields.[52,53] Then, compound **5** was cyclized with various triethylorthoesters in boiling acetic acid to give pyrido[1,2-*e*][1,2,4]triazolo[3,4-*b*]purine derivatives **6a−c** (Table 2). Moreover, conducting the reaction of compound **5** with acetic acid as an example of aliphatic acid under reflux conditions did not lead to the formation of 3-alkylpyrido[1,2-*e*][1,2,4]triazolo[3,4-*b*]purine even after 24 h.

Due to the regioselectivity of the cyclization reaction of compound **5** with triethylorthoesters, two-dimensional nuclear Overhauser effect spectroscopy (NOESY) is applied to determine which nitrogen atom on the pyrimidine core is cyclized with triethylorthoesters to form the corresponding triazole ring. The NOESY spectrum of compound **6c** reveals that there is no correlation between the hydrogens of the methyl group on the pyrimidine core (δ = 3.27 ppm) and the hydrogens of the methylene moiety on the triazole ring (δ = 3.06 ppm). As a result, the true regioisomer is the structure of **6a−c** (Figure 3).

On the contrary, the treatment of compound **5** with carbon disulfide in pyridine under reflux conditions afforded 5-methylpyrido[1,2-*e*][1,2,4]triazolo[3,4-*b*]purine-1(2*H*)-thione (**7**) in 63% yield. Consequently, the reaction of different alkyl halides with compound **7** in DMF at room temperature

Scheme 2. A Plausible Mechanism for Pyrido[1,2-*e*]purine Formation

Table 1. Construction of C-2-Substituted Pyrido[1,2-*e*]purines

Table 2. Synthetic Route for the Construction of 3-Alkyl-pyrido[1,2-*e*][1,2,4]triazolo[3,4-*b*]purines
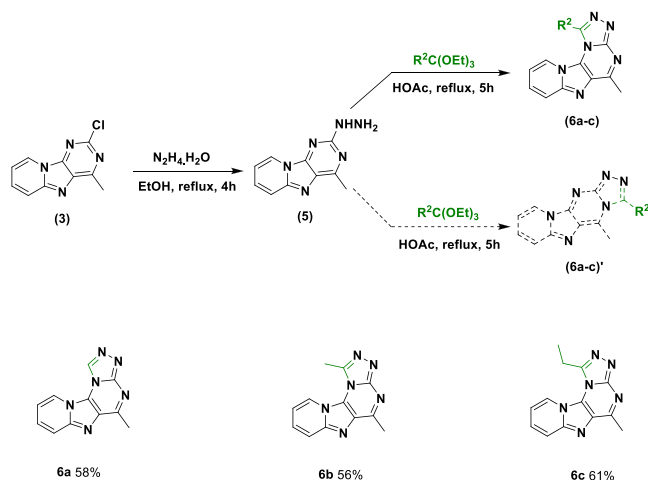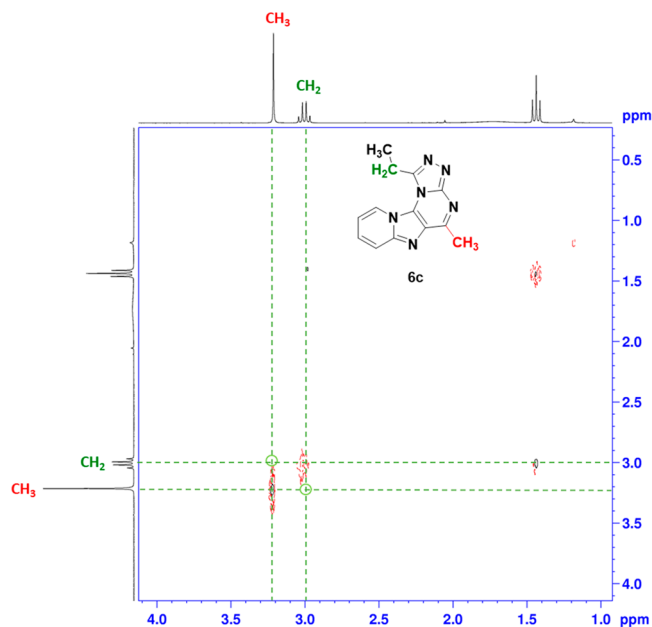
Figure 3. NOESY spectrum of compound **6c**.

interaction between the hydrogens of the methylene moiety of SEt and the hydrogens of the methyl group on the pyrimidine ring (see the Supporting Information).

Computational Analyses. The roles of computational approaches in drug discovery and evaluation of therapeutic behaviors of novel synthesized compounds are considerable. Computational tools do not have the limitation of animal models in investigating the synthesized compounds as safe drug candidates.[54] Also, an in silico molecular docking technique is used to study the biological activities by evaluating the interactions of the synthesized compounds with the corresponding active site. During a drug discovery process, pharmacokinetic problems have direct relations with the consumed costs and times. To overcome these issues, in silico physicochemical and pharmacokinetic investigations are necessary. Table 4 shows the calculated parameters by the SwissADME server,[55] including the number of the hydrogen-bond donors, the number of the hydrogen-bond acceptors, molecular weights, molar refractivities, logarithms of octanol/water partition coefficients (logP), and topological polar surface areas (TPSAs). Also, the results of PAINS (pan-assay interference compounds) analysis, applied to determine the possibility of a molecule being toxic, are reported in Table 4. Zero values of PAINS structural alerts signify a nontoxic nature for a typical compound.[56] The analyses are performed on the basis of the bioavailability applied during the procedure of drug design and discovery. Different rules have been provided to determine the bioavailability of the molecules.

However, Lipinski's rule of five is one of the best approaches for assessing appropriate membrane permeability, good oral bioavailability, and effective gastrointestinal absorption in the

produced the corresponding S-alkylated products **8a**−**g** in 68−80% yields (Table 3). Furthermore, the two-dimensional NOESY spectrum for compound **8b** as an example has been implemented to determine the regioselectivity of the cyclization reaction with carbon disulfide. The obtained result indicates no
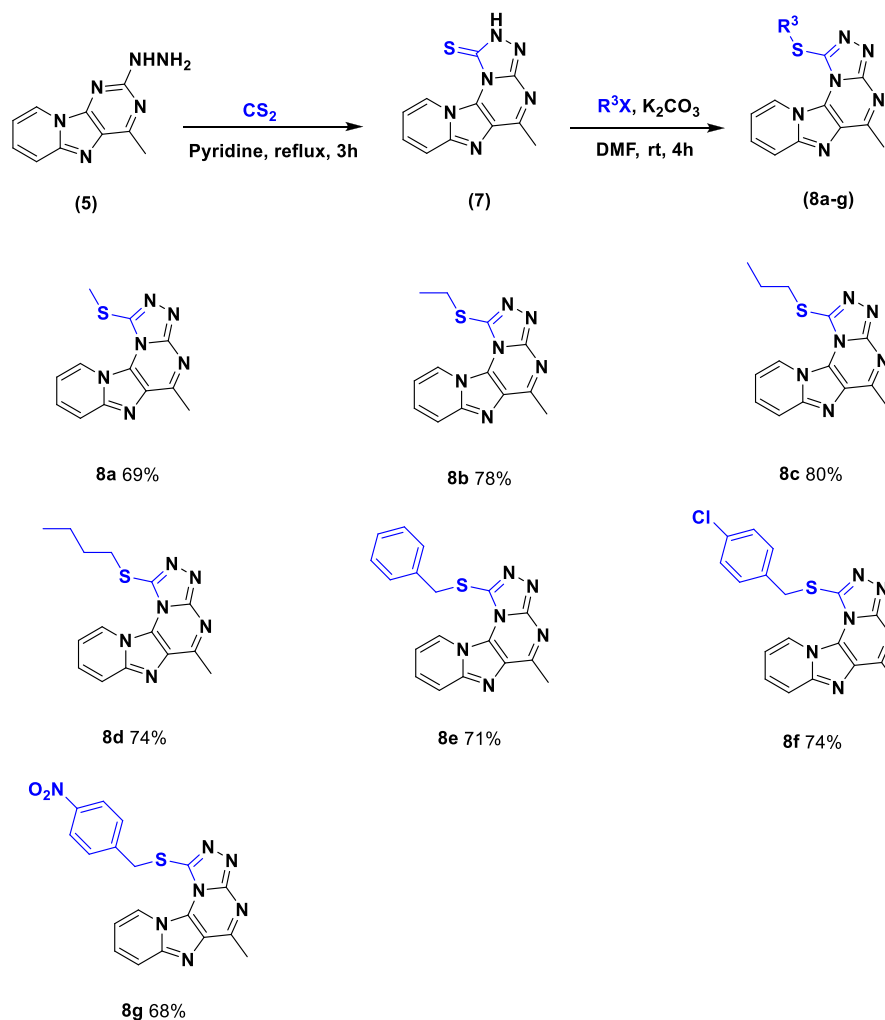
Table 3. Synthetic Route for the Construction of 1-(Alkylthio)pyrido[1,2-*e*][1,2,4]triazolo[3,4-*b*]purine

Table 4. Calculated Physicochemical Properties, Lipophilicities, Water Solubilities, Pharmacokinetics, Drug Likenesses, and Bioactivity Scores of the Synthesized Compounds by SwissADME

compound	log S (mol/L)	no. of heavy atoms	MW (g/mol)	no. of rotatable bonds	no. of H-bond acceptors	no. of H-bond donors	logP$_{o/w}$ (iLOGP)	molar refractivity	TPSA (Å^2)	bioavailability score	PAINS	Lipinski violation
4a	−3.36	20	269.30	1	4	0	2.86	78.98	55.55	0.55	0 alerts	0
4b	−3.84	19	253.30	1	3	0	2.98	77.90	46.32	0.55	0 alerts	0
4c	−4.12	20	267.33	1	3	0	3.05	82.70	46.32	0.55	0 alerts	0
4d	−4.46	21	281.36	1	3	0	3.22	87.51	46.32	0.55	0 alerts	0
4e	−3.54	21	282.34	1	4	0	3.21	89.51	49.56	0.55	0 alerts	0
4f	−3.77	22	296.37	2	4	0	3.47	94.32	49.56	0.55	0 alerts	0
6a	−3.51	17	224.22	0	4	0	1.83	62.00	60.38	0.55	0 alerts	0
6b	−3.82	18	238.25	0	4	0	2.06	66.97	60.38	0.55	0 alerts	0
6c	−4.08	19	252.27	1	4	0	2.30	71.78	60.38	0.55	0 alerts	0
7	−3.98	18	256.29	0	4	0	2.10	69.26	99.18	0.55	0 alerts	0
8a	−4.20	19	270.31	1	4	0	2.51	73.72	85.68	0.55	0 alerts	0
8b	−4.42	20	284.34	2	4	0	2.79	78.53	85.68	0.55	0 alerts	0
8c	−4.74	21	298.37	3	4	0	2.94	83.34	85.68	0.55	0 alerts	0
8d	−4.96	22	312.39	4	4	0	3.09	88.15	85.68	0.55	0 alerts	0
8e	−5.50	25	346.41	3	4	0	2.80	98.21	85.68	0.55	0 alerts	0
8f	−6.09	26	380.85	3	4	0	3.45	103.22	85.68	0.55	0 alerts	0
8g	−5.54	28	391.41	4	6	0	2.88	107.03	131.50	0.55	0 alerts	0

human abdomen. With regard to Lipinski's rule of five, good bioavailability for a typical compound is provided with a molecular weight (MW) of ≤500, a logP value of ≤4.15, ≤5 hydrogen-bond donors, and ≤10 hydrogen-bond acceptors.[57]

The Ghose rule suggests $160 \leq MW \leq 480$, $-0.4 \leq logP \leq 5.6$, $40 \leq$ molar refractivity (MR) ≤ 130, and $20 \leq n$ (number of atoms) ≤ 70 for compounds that have the appropriate good bioavailability. With regard to the Veber filter, good bioavailability is achieved when the number of rotatable bonds and the TPSA are ≤ 10 and ≤ 140 Å, respectively. On the basis of Egan's rule, a compound has significant bioavailability with a logP of ≤ 5.88 and a TPSA of ≤ 131 Å.[58] As shown in Table 4, the synthesized compounds do not show any violation of Lipinski's rule of five. Moreover, all compounds do not violate other rules, which illustrate their druglike potential.

One of the most applicable computer-assisted drug design methods is molecular docking implemented to discover the preferred orientation of ligands into protein active sites.[59] The purpose of the docking study is to understand the proper orientation of the pyrido[1,2-e]purine derivatives in the active site of the main protease of COVID-19. Yang and co-workers[60] reported the three-dimensional (3D) crystal structure of the main protease of SARS-CoV-2, and its complex with an inhibitor N3 has been deposited as RCSB Protein Data Bank entry 6LU7. After the inhibitor and water molecules had been removed, missing atoms were corrected with Chimera and Notepad++.[61] The improved 3D crystal structure of the main protease was subjected to a molecular docking investigation and molecular simulations. The amino acids in the binding site of the enzyme were determined by Cavityplus.[62] The specified amino acids were applied to determine a grid box in molecular docking investigations by AutoDock-Vina software. All synthesized molecules were optimized using Gaussian 09[63] at the B3LYP/6-31G(d,p) level of theory. For all of the docking investigations, the gride box size was 30 Å × 30 Å × 30 Å centralized on the respective geometric center. The Cartesian coordinates of the grid box were centered on the $x = -14.212$, $y = 19.133$, $z = 64.83$ coordinates of the enzyme. The energy calculations were evaluated using the genetic algorithms (GAs) for 20 geometry conformers. The results demonstrated that the structures had different interactions with the located amino acids in the active site of the enzyme. The interacting amino acids of all structures are listed in Table 5. The outcomes of the molecular docking revealed that compounds **4a** and **4c** have the lowest binding energy. Figure 4 illustrates the binding modes of compounds **4a** and **4c** and the interactions of amino acids.

Molecular Dynamics Simulation. After extraction of the final mode from the docking analyses for compounds **4a** and **4c**, the final models were simulated by the AMBER99SB-ILDN force field in Gromacs2020.[64] The docked complex was solvated in a cubic box with simple point charge (SPC) waters, and Na⁺ or Cl⁻ counterions were added to the system to achieve overall electrostatic neutrality. Long-range electrostatic interactions were evaluated by the particle mesh Ewald (PME) method, in which the cutoff distance was considered 1.2 Å for the long-range van der Waals (VDW) energy. During the simulation, the temperature was readjusted by using V-rescale. First, energy minimization of the whole system was performed without any restraints for 50000 interaction steps using the steepest descent algorithm. Then, the systems were equilibrated via two separate simulation steps. In the first step, the systems were equilibrated via a constant number of particles, volume, and temperature. The *NVT* ensemble protocol was used for the 200 ps simulation at 310 K, in which the Verlet scheme was utilized to control the temperature. In the same simulation time, the second phase of equilibration was carried out using a constant number of particles, pressure, and temperature (the *NPT* ensemble

Table 5. Docking Results of the Synthesized Compounds

compound	interacting residues	binding affinity (kcal/mol)
4a	Met165, Cys145, His41, Met49	−7.5
4b	Cys145, Leu27, Met165	−7.2
4c	Cys145, His41, Met49	−7.7
4d	Asn142, Leu141, Cys145, Met165, Met49, His41	−7.3
4e	Asn142, Phe140, Leu141, Met165, Met49, His41	−7.1
4f	Asn142, Phe140, Cys145, His41, Met165, Met49	−7.1
6a	Val104, Asp153, Phe294, Gln110, Ile106	−6.7
6b	Gln110, Phe8, Phe294, Val104, Ser158, Ile106	−7.0
6c	His41, Cys145, Met165, Gln189	−6.2
7	Asp153, Ile106, Ser158, Val104	−6.8
8a	Asn142, Cys145, His41, Met165, Met49, Asn142, Leu27	−6.3
8b	Cys145, His41, Met165, His163	−7.0
8c	Cys145, Met165, Leu27, His41, Asn142, Glu166	−6.8
8d	Cys145, His163, Met165, His41	−7.1
8e	Cys145, Ser144, His163, His172	−7.1
8f	Asn142, Cys145, Met49, Glu166, Met165	−7.2
8g	His41, Cys145, Met165, Glu166	−7.3

protocol) at 300 K, in which the Berendsen barostat and Verlet scheme were used to control the pressure (constant to 1 bar) and temperature, respectively. The LINCS algorithm was applied to covalent-bond restrictions in the equilibration steps. The ultimate production step was performed for 50000 ps of MD simulation at a constant temperature of 300 K, in which trajectories were saved every 1 fs.

Figure 5 depicts the root-mean-square deviations (RMSDs) of the protein for compounds **4a** and **4c** as the criteria for structural stability of the complexes during the simulation. RMSD values show the stability and conformational changes of the protein during the simulation. As shown in Figure 5, RMSD plots show that the main protease reached equilibrium after simulation for 3 ns and are stable up to 35000 ps. However, from 35000 to 45000 ps, the RMSD values increase and again decrease until 50000 ps. Both compounds **4a** and **4c** inhibit the increase in the RMSD values between 35000 and 45000 ps. The average RMSD values of the enzyme for complexes **4a** and **4c** are 0.23 and 0.21 nm, respectively. One can conclude that **4a** and **4c** compounds have remarkable effects on the stability of the enzyme. Also, the complex form of **4c** is more stable during the time of the simulation.

The radius of gyration (R_g) is a criterion for studying the compactness of the ligand−protein complex throughout the time of the molecular simulation. This factor evaluates the changes in distance between the center of mass of the protein atoms and its terminus. Generally, when the R_g of the ligand−protein complex is lower, the compactness of the complex becomes higher, which leads to stronger interactions between the ligand and protein. Also, the R_g value of a stable complex varies relatively less, which is a criterion of dynamic stability. Figure 6 depicts the variation of R_g of the ligand−protein complex versus the time of the simulation. The maximum values of R_g for **4a** and **4c** complexes occur at approximately 2.28 and 2.25 nm, respectively. However, after the maximum point, R_g values decrease during the simulation for both complexes. R_g values show that the binding of the compounds to the active site
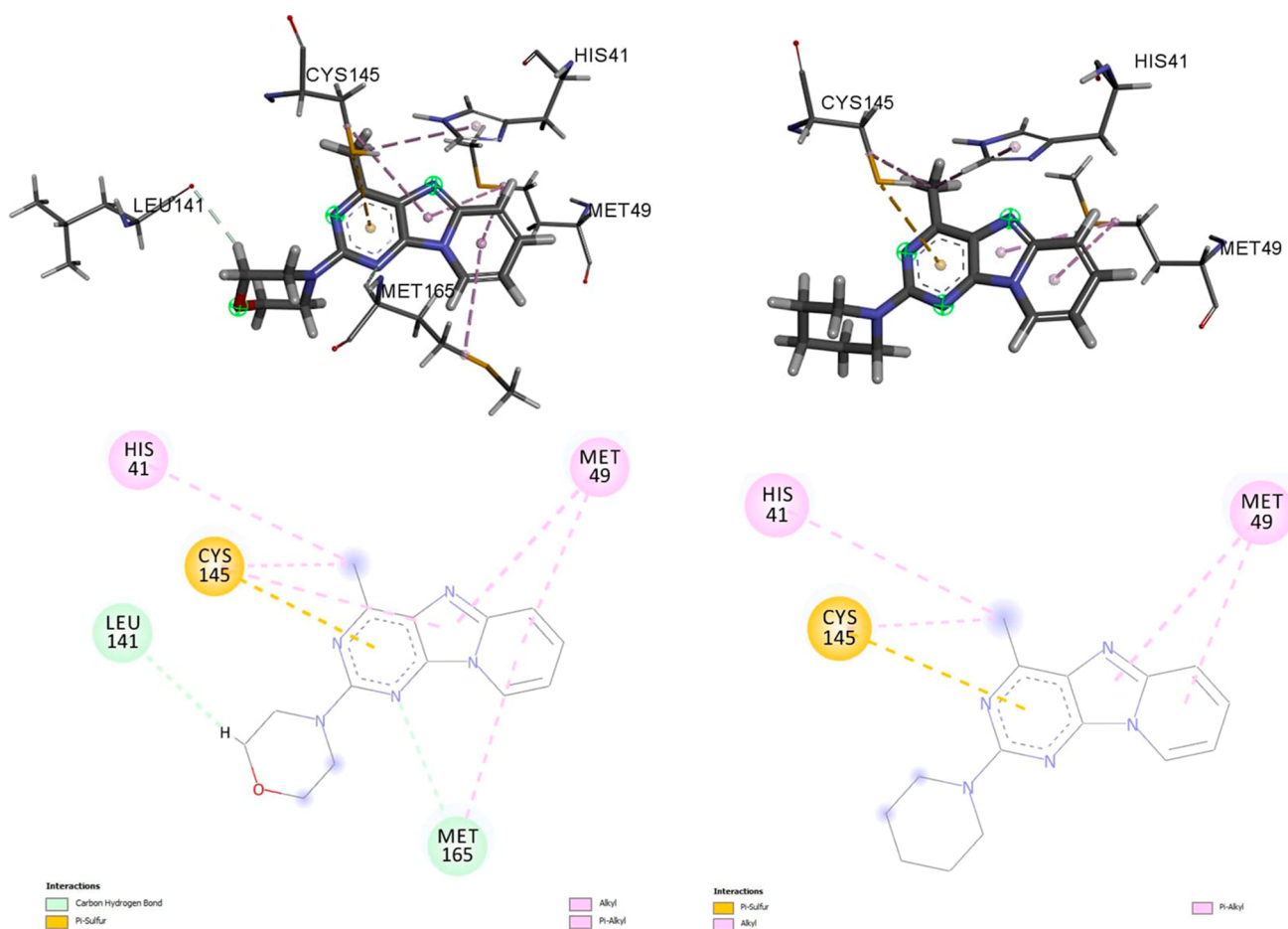
Figure 4. Interaction profile of the best-docked mode for compounds **4a** (left) and **4c** (right) and binding site interactions.
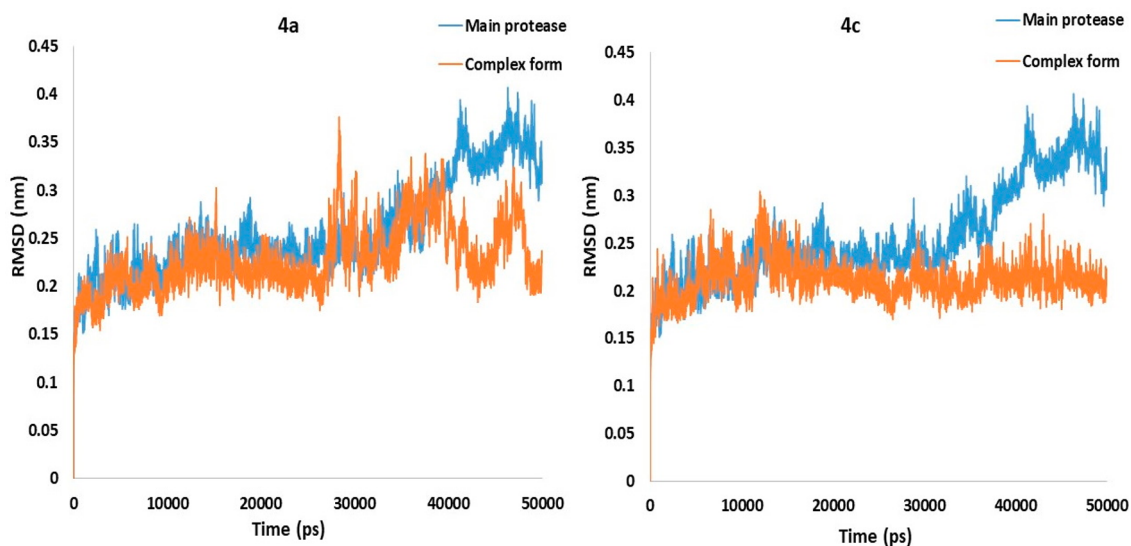

Figure 5. RMSD graph of the simulation of the main protease and complex that forms during a 50 ns simulation.

of the main protease does not induce remarkable variation in the conformational structure of the protein. On the contrary, the complexation of the main protease causes more compactness during the simulation.

A hydrogen bond (H-bond) is a key factor in determining the binding affinity and stabilization effect of the ligands with protein. The number and distribution of H-bonds in the

complexes were investigated to specify the stability of the system throughout the 50 ns simulation time. Thus, the average number of H-bonds during the MD phase makes a significant contribution to the stability of the ligand–protein complex. Figure 7 depicts the H-bond number results of **4a** and **4c** complexes that possess average H-bond numbers of 0.39 and 0.33 during a 50 ns simulation, respectively. Due to the oxygen
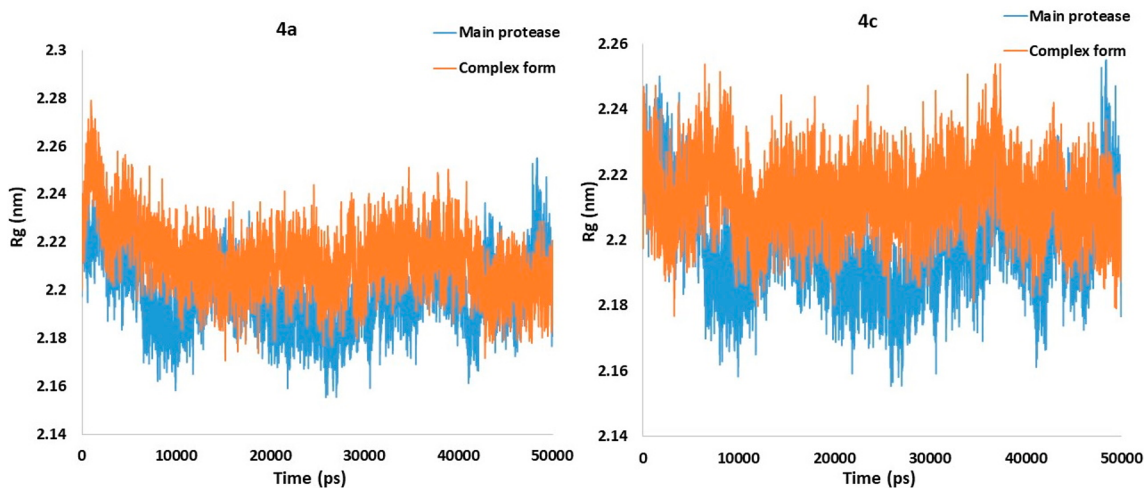
Figure 6. Plots of the radius of gyration (R_g) related to the compactness of **4a** and **4c** during a 50 ns simulation.
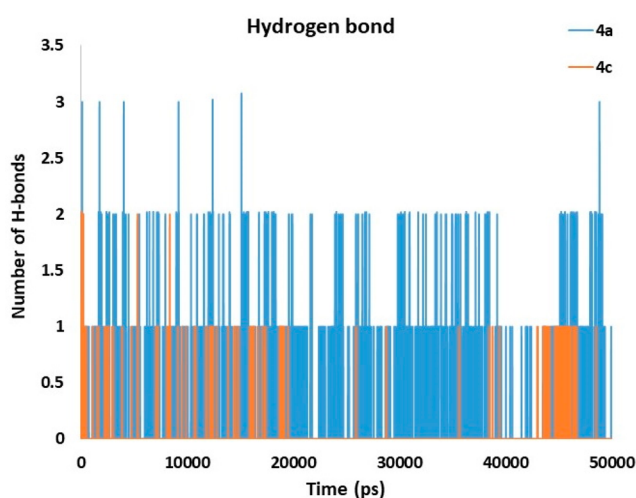

Figure 7. Hydrogen-bond (H-bond) results of **4a** and **4c** during a 50 ns simulation.

atom of the morpholine ring in **4a**, the average H-bond number in the corresponding complex is higher than that of **4c**.

To obtain a quantitative viewpoint, the study of free energy is helpful in the evaluation of the binding energy of the synthesized compounds in complexes with the enzyme. The molecular mechanics/Poisson−Boltzmann surface area (MMPBSA) method was used to determine the binding energies.[65,66] Different components of binding energies for the complexes of **4a** and **4c** were calculated by the g_mmpbsa application. The binding energy is composed of the average of three energetic parameters such as the binding free energy in a vacuum, polar solvation energy, and nonpolar solvation energy. In this study, snapshots taken every 1 ps between 45 and 50 ns were collected, and the MMPBSA method was carried out to evaluate the binding energy.

The results of MMPBSA studies (Table 6) show that the binding energy for complex **4a** is lower than that of complex **4c**. The energy of the solvent accessible surface area (SASA) and polar solvation energy have no remarkable effects on the total binding energy. However, the effects of van der Waals and electrostatic energies are more significant. Finally, one can conclude that the inhibitory effects of compound **4a** are more remarkable than those of compound **4c**.

■ CONCLUSION

In summary, a diverse library of pyrido[1,2-*e*]purine derivatives were prepared by a new two-step, one-pot pathway, including the reaction between pyridine and 2,4-dichloro-5-amino-6-methylpyrimidine under reflux conditions. The chlorine atom at the C-2 position can be directly replaced with various secondary amines as well as hydrazine hydrate, followed by cyclization with different triethylorthoesters and carbon disulfide to afford the desired products **4a−f**, **6a−c**, and **8a−g**. Different rules have been provided to distinguish the bioavailability of the prepared molecules, illustrating that the synthesized compounds do not show any toxicity or violation of Lipinski's rule of five. Due to these results, molecular docking and molecular dynamics simulation have been implemented to evaluate the inhibitory activity of the synthesized products against the main protease of COVID-19. On the basis of the molecular docking results, compounds **4a** and **4c** exhibited the highest binding affinities (−7.5 and −7.7 kcal/mol, respectively), which represent the favorable orientation in the active site of the chymotrypsin-like cysteine protease (3CL[pro]). After molecular docking, molecular dynamics simulations have been used to obtain more details about the ligand−protein complexes. The outcome of the MD simulation shows that the binding energy of complex **4a** is lower than that of complex **4c**, illustrating the inhibitory effects of compound **4a** are more significant than those of compound **4c**. Finally, the obtained results reveal that they can be used as

Table 6. van der Waals Energies, Polar Solvation Energies, Electrostatic Energies, and SASA Energy Components of the Total Binding Energy of Complexes 4a and 4c

	van der Waals energy (kJ/mol)	electrostatic energy (kJ/mol)	polar solvation energy (kJ/mol)	SASA energy (kJ/mol)	binding energy (kJ/mol)
4a	−141.746 ± 13.686	−32.295 ± 13.455	79.113 ± 9.153	−12.869 ± 1.039	−107.797 ± 13.827
4c	−109.878 ± 10.685	−11.316 ± 8.323	52.392 ± 6.638	−10.732 ± 0.951	−79.534 ± 9.731

G

suitable promising inhibitors of the main protease of SARS-CoV-2.

■ EXPERIMENTAL SECTION

Melting points were recorded using an Electrothermal-type 9200 melting point apparatus. The IR spectra were recorded using an Avatar 370 FT-IR Thermo Nicolet instrument, and only outstanding absorptions were listed. The ^{1}H NMR (300 MHz) and ^{13}C NMR (75 MHz) spectra were recorded using a Bruker Avance DRX-300 Fourier transform spectrometer. Chemical shifts were reported in parts per million downfield from tetramethylsilane (TMS) as an internal standard. The mass spectra were scanned using a Varian Mat CH-7 instrument at 70 eV.

Synthesis of 2-Chloro-4-methylpyrido[1,2-e]purine (3). 2,4-Dichloro-5-amino-6-methylpyrimidine (**2**) (1.78 g, 10 mmol) in pyridine (8 mL) was heated under reflux for 24 h. The progress of the reaction was monitored by TLC using a chloroform/methanol solvent (20:1). After the completion of the reaction, the solvent was evaporated under reduced pressure, and then water (10 mL) was added. The organic layer was extracted with CHCl$_3$ (3 × 15 mL) and dried over Na$_2$SO$_4$. The organic layer was evaporated under reduced pressure. The crude product was purified by column chromatography on silica gel (3:2 ethyl acetate/n-hexane eluent) to give the pure product: yellow solid (0.09 g, 44%); mp 195−198 °C; ^{1}H NMR (CDCl$_3$, 300 MHz) δ 8.65 (d, 1H, J = 6.0 Hz), 7.68−7.72 (m, 1H), 7.54−7.59 (m, 1H), 6.98 (t, 1H, J = 6.0 Hz), 2.97 (s, 3H); ^{13}C{^{1}H} NMR (CDCl$_3$, 75 MHz) δ 162.8, 151.0, 148.6, 146.4, 132.9, 132.5, 124.9, 118.9, 112.4, 20.1; IR (KBr discs, cm^{-1}) 2917, 1642, 1582, 1502, 1392, 1307, 1286, 1168; MS (m/z) 220 (M(^{37}Cl)$^{+}$), 218 (M(^{35}Cl)$^{+}$), 183 (M^{+} − Cl). Anal. Calcd for C$_{10}$H$_7$ClN$_4$: C, 54.93; H, 3.23; N, 25.63. Found: C, 54.72; H, 3.20; N, 25.35.

General Procedure for the Synthesis of 4a−f. A mixture of 2-chloro-4-methylpyrido[1,2-e]purine (**3**) (0.21 g, 1 mmol, 1 equiv) and the appropriate secondary amine (2 mmol, 2 equiv) in ethanol (3 mL) was stirred in an oil bath at 80 °C for 4−5 h. After the completion of the reaction, the solvent was evaporated, and the resulting precipitate was filtered off. The residue was recrystallized in ethanol to afford the desired product.

4-(4-Methylpyrido[1,2-e]purin-2-yl)morpholine (4a). Yellow soild (0.23 g, 88%); mp 108−110 °C; ^{1}H NMR (CDCl$_3$, 300 MHz) δ 8.43 (d, 1H, J = 6 Hz), 7.56 (d, 1H, J = 9 Hz), 7.30−7.36 (m, 1H), 6.77 (t, 1H, J = 6 Hz), 3.93 (t, 4H, J = 6 Hz), 3.84 (t, 4H, J = 6 Hz), 2.84 (s, 3H); ^{13}C{^{1}H} NMR (CDCl$_3$, 75 MHz) δ 160.9, 157.6, 146.5, 146.0, 129.6, 127.2, 124.2, 118.7, 110.7, 66.9, 45.1, 20.2; IR (KBr discs, cm^{-1}) 2958, 2853, 1638, 1609, 1581, 1384, 1113; MS (m/z) 269 (M^{+}), 182 (M^{+} − C$_4$H$_8$NO). Anal. Calcd for C$_{14}$H$_{15}$N$_5$O: C, 62.44; H, 5.61; N, 26.01. Found: C, 62.30; H, 5.58; N, 25.79.

4-Methyl-2-(pyrrolidin-1-yl)pyrido[1,2-e]purine (4b). Orange solid (0.21 g, 84%); mp 130−132 °C; ^{1}H NMR (CDCl$_3$, 300 MHz) δ 8.43 (d, 1H, J = 9 Hz), 7.53 (d, 1H, J = 9 Hz), 7.28−7.32 (m, 1H), 6.74 (t, 1H, J = 9 Hz), 3.69 (t, 4H, J = 6 Hz), 2.85 (s, 3H), 2.02−2.07 (m, 4H); ^{13}C{^{1}H} NMR (CDCl$_3$, 75 MHz) δ 160.8, 156.7, 146.8, 145.3, 129.0, 126.3, 124.3, 118.6, 110.3, 47.1, 25.6, 20.2; IR (KBr discs, cm^{-1}) 3105, 2962, 2864, 1636, 1605, 1577, 1526, 1381; MS (m/z) 253 (M^{+}), 182 (M^{+} − C$_4$H$_8$N). Anal. Calcd for C$_{14}$H$_{15}$N$_5$: C, 66.38; H, 5.97; N, 27.65. Found: C, 66.61; H, 5.91; N, 27.41.

4-Methyl-2-(piperidin-1-yl)pyrido[1,2-e]purine (4c). Pale yellow solid (0.24 g, 91%); mp 122−124 °C; ^{1}H NMR (CDCl$_3$, 300 MHz) δ 8.43 (d, 1H, J = 6 Hz), 7.54 (d, 1H, J = 12 Hz), 7.27−7.32 (m, 1H), 6.74 (t, 1H, J = 6 Hz), 3.92 (t, 4H, J = 6 Hz), 2.83 (s, 3H) 1.66−1.70 (m, 6H); ^{13}C{^{1}H} NMR (CDCl$_3$, 75 MHz) δ 160.8, 157.8, 146.7, 145.7, 129.2, 126.5, 124.3, 118.7, 110.4, 45.5, 25.8, 24.9, 20.3; IR (KBr discs, cm^{-1}) 3059, 2922, 2843, 1639, 1602, 1576, 1513, 1382, 1303; MS (m/z) 267 (M^{+}), 183 (M^{+} − C$_5$H$_{10}$N). Anal. Calcd for C$_{15}$H$_{17}$N$_5$: C, 67.39; H, 6.41; N, 26.20. Found: C, 67.21; H, 6.30; N, 26.34.

4-Methyl-2-(4-methylpiperidin-1-yl)pyrido[1,2-e]purine (4d). Pale yellow solid (0.24 g, 86%); mp 118−121 °C; ^{1}H NMR (CDCl$_3$, 300 MHz) δ 8.42 (d, 1H, J = 9 Hz), 7.52 (d, 1H, J = 9 Hz), 7.28−7.31 (m, 1H), 6.73 (t, 1H, J = 6 Hz), 4.85−4.92 (m, 2H), 2.88−2.97 (m, 2H),

2.81 (s, 3H), 1.65−1.78 (m, 3H), 1.20−1.29 (m, 2H), 0.98 (d, 3H, J = 6 Hz); ^{13}C{^{1}H} NMR (CDCl$_3$, 75 MHz) δ 160.8, 157.8, 146.8, 145.7, 129.2, 126.5, 124.3, 118.7, 110.5, 44.9, 34.1, 31.4, 22.0, 20.3; IR (KBr discs, cm^{-1}) 2919, 2847, 1640, 1605, 1580, 1512, 1384, 1314, 1220; MS (m/z) 281 (M^{+}), 183 (M^{+} − C$_6$H$_{12}$N). Anal. Calcd for C$_{16}$H$_{19}$N$_5$: C, 68.30; H, 6.81; N, 24.89. Found: C, 68.11; H, 6.69; N, 24.60.

4-Methyl-2-(4-methylpiperazin-1-yl)pyrido[1,2-e]purine (4e). Pale yellow solid (0.25 g, 92%); mp 117−119 °C; ^{1}H NMR (CDCl$_3$, 300 MHz) δ 8.41 (d, 1H, J = 6 Hz), 7.53 (d, 1H, J = 9 Hz), 7.30 (t, 1H, J = 9 Hz), 6.74 (t, 1H, J = 6 Hz), 3.96 (t, 4H, J = 6 Hz), 2.82 (s, 3H), 2.54 (t, 4H, J = 6 Hz), 2.37 (s, 3H); ^{13}C{^{1}H} NMR (CDCl$_3$, 75 MHz) δ 160.8, 157.6, 146.5, 145.9, 129.4, 126.9, 124.2, 118.7, 110.6, 55.0, 46.2, 44.4, 20.2; IR (KBr discs, cm^{-1}) 2929, 2790, 1638, 1607, 1583, 1513, 1384, 1308, 1006; MS (m/z) 282 (M^{+}), 183 (M^{+} − C$_5$H$_{11}$N$_2$). Anal. Calcd for C$_{15}$H$_{18}$N$_6$: C, 63.81; H, 6.43; N, 29.77. Found: C, 63.60; H, 6.38; N, 29.61.

2-(4-Ethylpiperazin-1-yl)-4-methylpyrido[1,2-e]purine (4f). Yellow solid (0.26 g, 89%); mp 120−123 °C; ^{1}H NMR (CDCl$_3$, 300 MHz) δ 8.42 (d, 1H, J = 6 Hz), 7.53 (d, 1H, J = 9 Hz), 7.29−7.33 (m, 1H), 6.74 (t, 1H, J = 6 Hz), 3.98 (t, 4H, J = 6 Hz), 2.82 (s, 3H), 2.59 (t, 4H, J = 6 Hz), 2.50 (q, 2H, J = 9 Hz), 1.16 (t, 3H, J = 9 Hz); ^{13}C{^{1}H} NMR (CDCl$_3$, 75 MHz) δ 160.9, 157.6, 146.6, 145.9, 129.4, 126.9, 124.3, 118.7, 110.6, 52.7, 44.4, 29.7, 20.2, 11.9; IR (KBr discs, cm^{-1}) 2922, 2852, 1638, 1611, 1582, 1510, 1387, 1307, 1226, 1012; MS (m/z) 296 (M^{+}), 183 (M^{+} − C$_6$H$_{13}$N$_2$). Anal. Calcd for C$_{16}$H$_{20}$N$_6$: C, 64.84; H, 6.80; N, 28.36. Found: C, 64.55; H, 6.67; N, 28.18.

2-Hydrazinyl-4-methylpyrido[1,2-e]purine (5). To 2-chloro-4-methylpyrido[1,2-e]purine (**3**) (0.65 g, 3 mmol) in ethanol (10 mL) was added hydrazine hydrate (3 mL), and the mixture was refluxed for 4 h. The progress of the reaction was monitored by TLC using a 10:1 chloroform/methanol eluent. After the completion of the reaction, the yellow precipitate was filtered off and washed with water (5 mL) and cold ethanol (5 mL). The residue was recrystallized from ethanol to afford the desired product: pale yellow solid (0.14 g, 68%); mp 236−238 °C; ^{1}H NMR (DMSO-d_6, 300 MHz) δ 8.54−8.57 (m, 1H), 7.58−7.61 (m, 1H), 7.46−7.49 (m, 1H), 6.93−6.98 (m, 1H), 2.69 (s, 3H); ^{13}C{^{1}H} NMR (DMSO-d_6, 75 MHz) δ 162.4, 150.5, 148.1, 145.9, 132.4, 132.0, 124.4, 118.5, 111.9, 19.65; IR (KBr discs) 3304, 3258, 3029, 2920, 1640, 1594, 1511, 1379, 1258, 940, 755; MS (m/z) 214 (M^{+}), 183 (M^{+} − N$_2$H$_3$). Anal. Calcd for C$_{10}$H$_{10}$N$_6$: C, 56.07; H, 4.71; N, 39.23. Found: C, 55.78; H, 4.59; N, 39.11.

General Procedure for the Synthesis of 6a−c. A mixture of 2-hydrazinyl-4-methylpyrido[1,2-e]purine (**5**) (0.21 g, 1 mmol, 1 equiv) and triethylorthoformate/acetate/propionate (2 mmol, 2 equiv) in glacial acetic acid (1 mL) was heated under reflux conditions for 5 h. After the completion of the reaction was monitored by TLC using a 20:1 chloroform/methanol eluent, the solvent was evaporated, and water (5 mL) was added. The pH was adjusted to ∼7 with a saturated NaHCO$_3$ solution, and the resulting precipitate was filtered off and recrystallized from ethanol.

5-Methylpyrido[1,2-e][1,2,4]triazolo[3,4-b]purine (6a). Pale yellow solid (0.12 g, 58%); mp 216−218 °C dec; ^{1}H NMR (CDCl$_3$, 300 MHz) δ 8.71 (d, 1H, J = 6 Hz), 8.60 (s, 1H), 7.57−7.61 (m, 2H), 6.92 (t, 1H, J = 6 Hz), 3.30 (s, 3H); ^{13}C{^{1}H} NMR (CDCl$_3$, 75 MHz) δ 156.1, 152.1, 151.5, 149.8, 140.6, 133.8, 132.2, 125.5, 118.5, 111.5, 13.4; IR (KBr discs, cm^{-1}) 3035, 2918, 1656, 1578, 1505, 1385, 1277; MS (m/z) 224 (M^{+}), 183 (M^{+} − CHN$_2$). Anal. Calcd for C$_{11}$H$_8$N$_6$: C, 58.92; H, 3.60; N, 37.48. Found: C, 58.72; H, 3.53; N, 37.24.

1,5-Dimethylpyrido[1,2-e][1,2,4]triazolo[3,4-b]purine (6b). Pale yellow solid (0.13 g, 56%); mp 267−270 °C dec; ^{1}H NMR (CDCl$_3$, 300 MHz) δ 8.69 (d, 1H, J = 6 Hz), 7.51−7.62 (m, 2H), 6.90 (t, 1H, J = 6 Hz), 3.26 (s, 3H), 2.72 (s, 3H); ^{13}C{^{1}H} NMR (CDCl$_3$, 75 MHz) δ 166.6, 152.7, 151.0, 145.2, 139.9, 133.3, 127.2, 125.5, 118.4, 111.3, 15.6, 13.4; IR (KBr discs, cm^{-1}) 3080, 2925, 1652, 1579, 1506, 1382, 1319, 1103; MS (m/z) 238 (M^{+}), 197 (M^{+} − C$_2$H$_3$N), 157 (M^{+} − C$_3$H$_3$N$_3$). Anal. Calcd for C$_{12}$H$_{10}$N$_6$: C, 60.50; H, 4.23; N, 35.27. Found: C, 60.69; H, 4.18; N, 35.04.

1-Ethyl-5-methylpyrido[1,2-e][1,2,4]triazolo[3,4-b]purine (6c). Pale yellow solid (0.15 g, 61%); mp 227−229 °C dec; ^{1}H NMR (CDCl$_3$, 300 MHz) δ 8.68 (d, 1H, J = 9 Hz), 7.51−7.63 (m, 2H), 6.90

(t, 1H, J = 6 Hz), 3.27 (s, 3H), 3.06 (q, 2H, J = 9 Hz), 1.50 (t, 3H, J = 9 Hz); ^{13}C{^{1}H} NMR (CDCl$_3$, 75 MHz) δ 171.3, 152.8, 150.9, 140.0, 133.3, 127.2, 125.5, 118.4, 111.2, 23.2, 13.4, 12.5; IR (KBr discs, cm^{-1}) 3041, 2982, 1653, 1579, 1506, 1382, 1105; MS (m/z) 252 (M$^+$), 223 (M$^+$ − C$_2$H$_5$), 197 (M$^+$ − C$_3$H$_5$N). Anal. Calcd for C$_{13}$H$_{12}$N$_6$: C, 61.89; H, 4.79; N, 33.31. Found: C, 61.63; H, 4.70; N, 33.16.

5-Methylpyrido[1,2-e][1,2,4]triazolo[3,4-b]purine-1(2H)-thione (7). To a suspension of 2-hydrazinyl-4-methylpyrido[1,2-e]purine (5) (0.21 g, 1 mmol) in pyridine (3 mL) was added carbon disulfide (1 mL). The mixture was refluxed in an oil bath for 4 h. The reaction progress was monitored by TLC using a 10:1 chloroform/methanol eluent. After the completion of the reaction, the solvent was evaporated and the orange residue was washed with water (10 mL) and recrystallized from aqueous dimethylformamide to afford the pure product: yellow solid (0.16 g, 63%); mp 239–242 °C; ^{1}H NMR (DMSO-d_6, 300 MHz) δ 8.67 (d, 1H, J = 9 Hz), 7.52–7.65 (m, 2H), 6.92 (t, 1H, J = 6 Hz), 3.25 (s, 3H); ^{13}C{^{1}H} NMR (DMSO-d_6, 75 MHz) δ 168.8, 152.5, 150.7, 144.5, 139.5, 133.0, 126.8, 125.2, 118.3, 111.4, 13.3; IR (KBr discs, cm^{-1}) 3296, 3080, 2597, 1654, 1571, 1503, 1389, 1327, 1198; MS (m/z) 256 (M$^+$), 223 (M$^+$ − SH), 197 (M$^+$ − CHNS). Anal. Calcd for C$_{11}$H$_8$N$_6$S: C, 51.55; H, 3.15; N, 32.79; S, 12.51. Found: C, 51.29; H, 3.09; N, 32.57; S, 12.33.

General Procedure for the Synthesis of 8a−g. To a solution of 5-methylpyrido[1,2-e][1,2,4]triazolo[3,4-b]purine-1(2H)-thione (7) (0.25 g, 1 mmol, 1 equiv) in DMF (3 mL) was added K$_2$CO$_3$ (0.13 g, 1 mmol, 1 equiv) at room temperature. After the mixture had been stirred for 30 min, the appropriate alkyl halide (1 mmol, 1 equiv) was added, and the mixture was stirred at room temperature for 4 h. After the completion of the reaction monitored by TLC using a 30:1 chloroform/methanol solvent, cold water (5 mL) was added. The mixture was neutralized with 5% HCl, and the precipitate was filtered, washed with water (5 mL), and recrystallized from ethanol.

5-Methyl-1-(methylthio)pyrido[1,2-e][1,2,4]triazolo[3,4-b]purine (8a). Yellow solid (0.18 g, 69%); mp 226–229 °C; ^{1}H NMR (CDCl$_3$, 300 MHz) δ 8.59 (d, 1H, J = 9 Hz), 7.44–7.57 (m, 2H), 6.84 (t, 1H, J = 6 Hz), 3.17 (s, 3H), 2.72 (s, 3H); ^{13}C{^{1}H} NMR (CDCl$_3$, 75 MHz) δ 168.3, 152.1, 150.3, 139.1, 132.7, 126.4, 124.8, 117.9, 111.1, 14.8, 13.0; IR (KBr discs, cm^{-1}) 3082, 2926, 1658, 1598, 1503, 1376, 1281, 1094; MS (m/z) 270 (M$^+$), 223 (M$^+$ − SMe), 197 (M$^+$ − C$_2$H$_3$NS). Anal. Calcd for C$_{12}$H$_{10}$N$_6$S: C, 53.32; H, 3.73; N, 31.09; S, 11.86. Found: C, 53.17; H, 3.64; N, 30.86; S, 11.61.

1-(Ethylthio)-5-methylpyrido[1,2-e][1,2,4]triazolo[3,4-b]purine (8b). Green solid (0.22 g, 78%); mp 245–247 °C; ^{1}H NMR (CDCl$_3$, 300 MHz) δ 8.66 (d, 1H, J = 6 Hz), 7.51–7.63 (m, 2H), 6.91 (t, 1H, J = 6 Hz), 3.37 (q, 2H, J = 6 Hz), 3.23 (s, 3H), 1.52 (t, 3H, J = 6 Hz); ^{13}C{^{1}H} NMR (CDCl$_3$, 75 MHz) δ 168.8, 152.6, 150.7, 139.6, 133.2, 126.8, 125.3, 118.4, 111.6, 25.8, 15.3, 13.4; IR (KBr discs) 3080, 2966, 1648, 1574, 1542, 1504, 1349, 1305; MS (m/z) 284 (M$^+$), 223 (M$^+$ − C$_2$H$_5$S), 197 (M$^+$ − C$_3$H$_5$NS). Anal. Calcd for C$_{13}$H$_{12}$N$_6$S: C, 54.91; H, 4.25; N, 29.56; S, 11.28. Found: C, 55.10; H, 4.12; N, 29.79; S, 11.13.

5-Methyl-1-(propylthio)pyrido[1,2-e][1,2,4]triazolo[3,4-b]purine (8c). Green solid (0.23 g, 80%); mp 210–213 °C; ^{1}H NMR (CDCl$_3$, 300 MHz) δ 8.63 (d, 1H, J = 9 Hz), 7.49–7.60 (m, 2H), 6.89 (t, 1H, J = 6 Hz), 3.33 (t, 2H, J = 6 Hz), 3.21 (s, 3H), 1.81–1.93 (m, 2H), 1.08 (t, 3H, J = 6 Hz); ^{13}C{^{1}H} NMR (CDCl$_3$, 75 MHz) δ 168.9, 152.5, 150.7, 144.5, 139.6, 133.1, 126.9, 125.3, 118.4, 111.5, 33.4, 29.7, 23.3, 13.4; IR (KBr discs, cm^{-1}) 3088, 2962, 1651, 1572, 1542, 1505, 1350, 1282; MS (m/z) 298 (M$^+$), 255 (M$^+$ − C$_3$H$_7$), 197 (M$^+$ − C$_4$H$_7$NS). Anal. Calcd for C$_{14}$H$_{14}$N$_6$S: C, 56.36; H, 4.73; N, 28.17; S, 10.75. Found: C, 56.09; H, 4.62; N, 27.99; S, 11.01.

1-(Butylthio)-5-methylpyrido[1,2-e][1,2,4]triazolo[3,4-b]purine (8d). Green solid (0.23 g, 74%); mp 191–193 °C dec; ^{1}H NMR (CDCl$_3$, 300 MHz) δ 8.67 (d, 1H, J = 6 Hz), 7.51–7.63 (m, 2H), 6.91 (t, 1H, J = 6 Hz), 3.37 (t, 2H, J = 6 Hz), 3.23 (s, 3H), 1.79–1.89 (m, 2H), 1.47–1.59 (m, 2H), 0.97 (t, 3H, J = 6 Hz); ^{13}C{^{1}H} NMR (CDCl$_3$, 75 MHz) δ 169.0, 152.6, 150.8, 144.6, 139.6, 133.1, 127.0, 125.3, 118.4, 111.5, 31.9, 31.2, 21.9, 13.6, 13.4; IR (KBr discs, cm^{-1}) 3088, 2958, 1651, 1579, 1545, 1348, 1302, 1281; MS (m/z) 312 (M$^+$), 297 (M$^+$ − CH$_3$), 223 (M$^+$ − C$_4$H$_9$S). Anal. Calcd for C$_{15}$H$_{16}$N$_6$S: C,

57.67; H, 5.16; N, 26.90; S, 10.26. Found: C, 57.51; H, 5.11; N, 27.15; S, 10.17.

1-(Benzylthio)-5-methylpyrido[1,2-e][1,2,4]triazolo[3,4-b]purine (8e). Yellow solid (0.24 g, 71%); mp 230–232 °C; ^{1}H NMR (CDCl$_3$, 300 MHz) δ 8.74 (d, 1H, J = 6 Hz), 7.66–7.76 (m, 2H), 7.51–7.54 (m, 2H), 7.30–7.35 (m, 3H), 7.02 (t, 1H, J = 6 Hz), 4.63 (s, 2H), 3.29 (s, 3H); ^{13}C{^{1}H} NMR (CDCl$_3$, 75 MHz) δ 168.2, 152.5, 150.9, 139.7, 137.4, 133.2, 129.1, 128.9, 128.5, 128.4, 127.7, 127.4, 127.0, 125.3, 118.4, 111.5, 35.7, 13.4; IR (KBr discs, cm^{-1}) 3039, 2919, 1652, 1577, 1543, 1505, 1353, 1283; MS (m/z) 346 (M$^+$), 223 (M$^+$ − C$_7$H$_7$S), 197 (M$^+$ − C$_8$H$_7$NS). Anal. Calcd for C$_{18}$H$_{14}$N$_6$S: C, 62.41; H, 4.07; N, 24.26; S, 9.25. Found: C, 62.60; H, 4.00; N, 24.16; S, 9.32.

1-[(4-Chlorobenzyl)thio]-5-methylpyrido[1,2-e][1,2,4]triazolo-[3,4-b]purine (8f). Green solid (0.28 g, 74%); mp 263–265 °C; ^{1}H NMR (CDCl$_3$, 300 MHz) δ 8.68 (d, 1H, J = 6 Hz), 7.53–7.64 (m, 3H), 7.45–7.48 (m, 2H), 6.91–7.02 (m, 2H), 4.57 (s, 2H), 3.23 (s, 3H); ^{13}C{^{1}H} NMR (CDCl$_3$, 75 MHz) δ 167.7, 151.0, 139.8, 136.2, 133.3, 133.2, 132.5, 130.5, 128.6, 127.1, 125.3, 124.9, 119.0, 118.5, 112.4, 111.6, 34.9, 13.4; IR (KBr discs, cm^{-1}) 3039, 2911, 1648, 1570, 1542, 1504, 1349, 1281; MS (m/z) 380 (M$^+$), 223 (M$^+$ − C$_7$H$_6$ClS), 197 (M$^+$ − C$_8$H$_6$ClNS). Anal. Calcd for C$_{18}$H$_{13}$ClN$_6$S: C, 56.77; H, 3.44; N, 22.07; S, 8.42. Found: C, 56.64; H, 3.39; N, 22.19; S, 8.34.

5-Methyl-1-[(4-nitrobenzyl)thio]pyrido[1,2-e][1,2,4]triazolo[3,4-b]purine (8g). Yellow solid (0.26 g, 68%); mp 278–280 °C; ^{1}H NMR (CDCl$_3$, 300 MHz) δ 8.68 (d, 1H, J = 9 Hz), 8.16 (d, 2H, J = 9 Hz), 7.72 (d, 2H, J = 9 Hz), 7.59–7.65 (m, 2H), 6.92–6.98 (m, 1H), 4.67 (s, 2H), 3.23 (s, 3H); ^{13}C{^{1}H} NMR (CDCl$_3$, 75 MHz) δ 167.8, 151.0, 139.8, 136.2, 133.4, 133.2, 132.6, 130.5, 128.7, 127.2, 125.4, 124.9, 119.0, 118.5, 112.5, 111.6, 35.0, 13.5; IR (KBr discs, cm^{-1}) 3082, 2926, 1652, 1574, 1542, 1501, 1352, 1305; MS (m/z) 391 (M$^+$), 222 (M$^+$ − C$_7$H$_6$NO$_2$S), 197 (M$^+$ − C$_8$H$_6$N$_2$O$_2$S). Anal. Calcd for C$_{18}$H$_{13}$N$_7$O$_2$S: C, 55.24; H, 3.35; N, 25.05; S, 8.19. Found: C, 55.41; H, 3.29; N, 24.90; S, 8.12.

■ ASSOCIATED CONTENT

ⓢ Supporting Information

The Supporting Information is available free of charge at https://pubs.acs.org/doi/10.1021/acs.joc.1c02237.

    Copies of ^{1}H and ^{13}C{^{1}H} spectra of all of the synthesized compounds and NOESY spectrum of compound **8b** (PDF)

Accession Codes

CCDC 2109260 contains the supplementary crystallographic data for this paper. These data can be obtained free of charge via www.ccdc.cam.ac.uk/data_request/cif, or by emailing data_request@ccdc.cam.ac.uk, or by contacting The Cambridge Crystallographic Data Centre, 12 Union Road, Cambridge CB2 1EZ, UK; fax: +44 1223 336033.

■ AUTHOR INFORMATION

Corresponding Author

Ali Shiri − *Department of Chemistry, Faculty of Science, Ferdowsi University of Mashhad, Mashhad, Iran;* ⓘ orcid.org/0000-0002-5736-6287; Email: alishiri@um.ac.ir

Authors

Parvin Moghimi − *Department of Chemistry, Faculty of Science, Ferdowsi University of Mashhad, Mashhad, Iran;* ⓘ orcid.org/0000-0002-5583-2117

Hossein Sabet-Sarvestani − *Department of Chemistry, Faculty of Science, Ferdowsi University of Mashhad, Mashhad, Iran;* ⓘ orcid.org/0000-0002-5461-2868

Omid Kohandel − *Department of Chemistry, Faculty of Science, Ferdowsi University of Mashhad, Mashhad, Iran*

■ REFERENCES

(1) Wu, F.; Zhao, S.; Yu, B.; Chen, Y.-M.; Wang, W.; Song, Z.-G.; Hu, Y.; Tao, Z.-W.; Tian, J.-H.; Pei, Y.-Y.; et al. A New Coronavirus Associated with Human Respiratory Disease in China. *Nature* **2020**, *579* (7798), 265−269.

(2) Liu, C.; Zhou, Q.; Li, Y.; Garner, L. V.; Watkins, S. P.; Carter, L. J.; Smoot, J.; Gregg, A. C.; Daniels, A. D.; Jervey, S.; Albaiu, D. Research and Development on Therapeutic Agents and Vaccines for COVID-19 and Related Human Coronavirus Diseases. *ACS Cent. Sci.* **2020**, *6* (3), 315−331.

(3) Wang, H.; Li, X.; Li, T.; Zhang, S.; Wang, L.; Wu, X.; Liu, J. The Genetic Sequence, Origin, and Diagnosis of SARS-CoV-2. *Eur. J. Clin. Microbiol. Infect. Dis.* **2020**, *39* (9), 1629−1635.

(4) Huang, J.; Song, W.; Huang, H.; Sun, Q. Pharmacological Therapeutics Targeting RNA-Dependent RNA Polymerase, Proteinase and Spike Protein: From Mechanistic Studies to Clinical Trials for COVID-19. *J. Clin. Med.* **2020**, *9* (4), 1131.

(5) Wang, F.; Chen, C.; Tan, W.; Yang, K.; Yang, H. Structure of Main Protease from Human Coronavirus NL63: Insights for Wide Spectrum Anti-Coronavirus Drug Design. *Sci. Rep.* **2016**, *6* (1), 22677.

(6) Zhang, L.; Lin, D.; Sun, X.; Curth, U.; Drosten, C.; Sauerhering, L.; Becker, S.; Rox, K.; Hilgenfeld, R. Crystal Structure of SARS-CoV-2 Main Protease Provides a Basis for Design of Improved α-Ketoamide Inhibitors. *Science.* **2020**, *368* (6489), 409−412.

(7) Ren, Z.; Yan, L.; Zhang, N.; Guo, Y.; Yang, C.; Lou, Z.; Rao, Z. The Newly Emerged SARS-like Coronavirus HCoV-EMC Also Has an" Achilles' Heel": Current Effective Inhibitor Targeting a 3C-like Protease. *Protein Cell* **2013**, *4* (4), 248−250.

(8) Zhang, L.; Lin, D.; Kusov, Y.; Nian, Y.; Ma, Q.; Wang, J.; Von Brunn, A.; Leyssen, P.; Lanko, K.; Neyts, J.; de Wilde, A.; Snijder, E. J.; Liu, H.; Hilgenfeld, R. α-Ketoamides as Broad-Spectrum Inhibitors of Coronavirus and Enterovirus Replication: Structure-Based Design, Synthesis, and Activity Assessment. *J. Med. Chem.* **2020**, *63* (9), 4562−4578.

(9) Verma, N.; Henderson, J. A.; Shen, J. Proton-Coupled Conformational Activation of SARS Coronavirus Main Proteases and Opportunity for Designing Small-Molecule Broad-Spectrum Targeted Covalent Inhibitors. *J. Am. Chem. Soc.* **2020**, *142* (52), 21883−21890.

(10) Thanigaimalai, P.; Konno, S.; Yamamoto, T.; Koiwai, Y.; Taguchi, A.; Takayama, K.; Yakushiji, F.; Akaji, K.; Chen, S. E.; Naser-Tavakolian, A.; et al. Development of Potent Dipeptide-Type SARS-CoV 3CL Protease Inhibitors with Novel P3 Scaffolds: Design, Synthesis, Biological Evaluation, and Docking Studies. *Eur. J. Med. Chem.* **2013**, *68*, 372−384.

(11) Frecer, V.; Miertus, S. Antiviral Agents against COVID-19: Structure-Based Design of Specific Peptidomimetic Inhibitors of SARS-CoV-2 Main Protease. *RSC Adv.* **2020**, *10* (66), 40244−40263.

(12) Zhang, C. H.; Spasov, K. A.; Reilly, R. A.; Hollander, K.; Stone, E. A.; Ippolito, J. A.; Liosi, M. E.; Deshmukh, M. G.; Tirado-Rives, J.; Zhang, S.; Liang, Z.; Miller, S. J.; Isaacs, F.; Lindenbach, B. D.; Anderson, K. S.; Jorgensen, W. L. Optimization of Triarylpyridinone Inhibitors of the Main Protease of SARS-CoV-2 to Low-Nanomolar Antiviral Potency. *ACS Med. Chem. Lett.* **2021**, *12* (8), 1325−1332.

(13) Assis, L. C.; de Castro, A. A.; de Jesus, J. P. A.; Nepovimova, E.; Kuca, K.; Ramalho, T. C.; La Porta, F. A. Computational Evidence for Nitro Derivatives of Quinoline and Quinoline N-Oxide as Low-Cost Alternative for the Treatment of SARS-CoV-2 Infection. *Sci. Rep.* **2021**, *11* (1), 6397.

(14) Liu, P.; Liu, H.; Sun, Q.; Liang, H.; Li, C.; Deng, X.; Liu, Y.; Lai, L. Potent Inhibitors of SARS-CoV-2 3C-like Protease Derived from N-Substituted Isatin Compounds. *Eur. J. Med. Chem.* **2020**, *206*, 112702.

(15) Llanes, A.; Cruz, H.; Nguyen, V. D.; Larionov, O. V.; Fernández, P. L. A Computational Approach to Explore the Interaction of Semisynthetic Nitrogenous Heterocyclic Compounds with the SARS-CoV-2 Main Protease. *Biomolecules* **2021**, *11* (1), 18−31.

(16) Ton, A. T.; Gentile, F.; Hsing, M.; Ban, F.; Cherkasov, A. Rapid Identification of Potential Inhibitors of SARS-CoV-2 Main Protease by Deep Docking of 1.3 Billion Compounds. *Mol. Inform.* **2020**, *39* (8), 2000028.

(17) Hou, X.; Majik, M. S.; Kim, K.; Pyee, Y.; Lee, Y.; Alexander, V.; Chung, H.-J.; Lee, H. W.; Chandra, G.; Lee, J. H.; et al. Structure-Activity Relationships of Truncated C2-or C8-Substituted Adenosine Derivatives as Dual Acting A2A and A3 Adenosine Receptor Ligands. *J. Med. Chem.* **2012**, *55* (1), 342−356.

(18) Xie, M.-S.; Chu, Z.-L.; Niu, H.-Y.; Qu, G.-R.; Guo, H. M. A Copper-Catalyzed Domino Route toward Purine-Fused Tricyclic Derivatives. *J. Org. Chem.* **2014**, *79* (3), 1093−1099.

(19) Song, Y.; Lin, X.; Kang, D.; Li, X.; Zhan, P.; Liu, X.; Zhang, Q. Discovery and Characterization of Novel Imidazopyridine Derivative CHEQ-2 as a Potent CDC25 Inhibitor and Promising Anticancer Drug Candidate. *Eur. J. Med. Chem.* **2014**, *82*, 293−307.

(20) Suma, V. R.; Sreenivasulu, R.; Rao, M. V. B.; Subramanyam, M.; Ahsan, M. J.; Alluri, R.; Rao, K. R. M. Design, Synthesis, and Biological Evaluation of Chalcone-Linked Thiazole-Imidazopyridine Derivatives as Anticancer Agents. *Med. Chem. Res.* **2020**, *29* (9), 1643−1654.

(21) Ehmke, V.; Winkler, E.; Banner, D. W.; Haap, W.; Schweizer, W. B.; Rottmann, M.; Kaiser, M.; Freymond, C.; Schirmeister, T.; Diederich, F. Optimization of Triazine Nitriles as Rhodesain Inhibitors: Structure-Activity Relationships, Bioisosteric Imidazopyridine Nitriles, and X-ray Crystal Structure Analysis with Human Cathepsin L. *ChemMedChem* **2013**, *8* (6), 967−975.

(22) Feng, S.; Hong, D.; Wang, B.; Zheng, X.; Miao, K.; Wang, L.; Yun, H.; Gao, L.; Zhao, S.; Shen, H. C. Discovery of Imidazopyridine Derivatives as Highly Potent Respiratory Syncytial Virus Fusion Inhibitors. *ACS Med. Chem. Lett.* **2015**, *6* (3), 359−362.

(23) Chen, G.; Liu, Z.; Zhang, Y.; Shan, X.; Jiang, L.; Zhao, Y.; He, W.; Feng, Z.; Yang, S.; Liang, G. Synthesis and Anti-Inflammatory Evaluation of Novel Benzimidazole and Imidazopyridine Derivatives. *ACS Med. Chem. Lett.* **2013**, *4* (1), 69−74.

(24) Azimi, S.; Zonouzi, A.; Firuzi, O.; Iraji, A.; Saeedi, M.; Mahdavi, M.; Edraki, N. Discovery of Imidazopyridines Containing Isoindoline-1, 3-Dione Framework as a New Class of BACE1 Inhibitors: Design, Synthesis and SAR Analysis. *Eur. J. Med. Chem.* **2017**, *138*, 729−737.

(25) Li, R. L.; Liang, L.; Xie, M.-S.; Qu, G. R.; Niu, H.-Y.; Guo, H. M. Copper-Catalyzed Intramolecular Cyclization of N-Propargyl-Adenine: Synthesis of Purine-Fused Tricyclics. *J. Org. Chem.* **2014**, *79* (8), 3665−3670.

(26) Zhao, L.; Christov, P. P.; Kozekov, I. D.; Pence, M. G.; Pallan, P. S.; Rizzo, C. J.; Egli, M.; Guengerich, F. P. Replication of N2, 3-ethenoguanine by DNA Polymerases. *Angew. Chemie Int. Ed.* **2012**, *51* (22), 5466−5469.

(27) Castillo, J. C.; Estupiñan, D.; Nogueras, M.; Cobo, J.; Portilla, J. 6-(Aryldiazenyl) Pyrazolo [1, 5-a] Pyrimidines as Strategic Intermediates for the Synthesis of Pyrazolo [5, 1-b] Purines. *J. Org. Chem.* **2016**, *81* (24), 12364−12373.

(28) Chen, C.; Chang, Y.; Bau, D.; Huang, H.; Tsai, F.; Tsai, C.; Chen, C. Y. Discovery of Potent Inhibitors for Phosphodiesterase 5 by Virtual Screening and Pharmacophore Analysis. *Acta Pharmacol. Sin.* **2009**, *30* (8), 1186−1194.

(29) Srivani, P.; Srinivas, E.; Raghu, R.; Sastry, G. N. Molecular Modeling Studies of Pyridopurinone Derivatives—Potential Phosphodiesterase 5 Inhibitors. *J. Mol. Graph. Model.* **2007**, *26* (1), 378−390.

(30) Xia, G.; Li, J.; Peng, A.; Lai, S.; Zhang, S.; Shen, J.; Liu, Z.; Chen, X.; Ji, R. Synthesis and Phosphodiesterase 5 Inhibitory Activity of Novel

Pyrido [1, 2-e] Purin-4 (3H)-One Derivatives. *Bioorg. Med. Chem. Lett.* **2005**, *15* (11), 2790−2794.

(31) Chaudhary, V.; Das, S.; Nayak, A.; Guchhait, S. K.; Kundu, C. N. Scaffold-Hopping and Hybridization Based Design and Building Block Strategic Synthesis of Pyridine-Annulated Purines: Discovery of Novel Apoptotic Anticancer Agents. *RSC Adv.* **2015**, *5* (33), 26051−26060.

(32) Favier, A.; Blackledge, M.; Simorre, J.-P.; Crouzy, S.; Dabouis, V.; Gueiffier, A.; Marion, D.; Debouzy, J.-C. Solution Structure of 2-(Pyrido [1, 2-e] Purin-4-Yl) Amino-Ethanol Intercalated in the DNA Duplex d (CGATCG) 2. *Biochemistry* **2001**, *40* (30), 8717−8726.

(33) Pericherla, K.; Kaswan, P.; Pandey, K.; Kumar, A. Recent Developments in the Synthesis of Imidazo [1, 2-a] Pyridines. *Synthesis (Stuttg).* **2015**, *47* (07), 887−912.

(34) Tber, Z.; Biteau, N.; Agrofoglio, L.; Cros, J.; Goffinont, S.; Castaing, B.; Nicolas, C.; Roy, V. Microwave-Assisted Suzuki-Miyaura and Sonogashira Coupling of 4-Chloro-2-(Trifluoromethyl) Pyrido [1, 2-e] Purine Derivatives. *Eur. J. Org. Chem.* **2019**, *2019* (33), 5756−5767.

(35) Marzouk, V. H. R.; Hennum, M.; Gundersen, L.-L. Efficient Synthesis of Cytotoxic Pyrido [1, 2-e] Purines from Purines Employing Direct C-Allylation and RCM-Oxidation as Key Steps. *Tetrahedron Lett.* **2013**, *54* (26), 3437−3439.

(36) Raji Reddy, C.; Burra, A. G. [4+ 2]-Annulation of MBH-Acetates of Acetylenic Aldehydes with Imidazoles/Benzimidazoles To Access Imidazo [1, 2-a] Pyridines/Benzimidazo [1, 2-a] Pyridines. *J. Org. Chem.* **2019**, *84* (14), 9169−9178.

(37) Cerna, I.; Pohl, R.; Klepetarova, B.; Hocek, M. Intramolecular Direct C- H Arylation Approach to Fused Purines. Synthesis of Purino [8, 9-f] Phenanthridines and 5,6-Dihydropurino [8,9-a] Isoquinolines. *J. Org. Chem.* **2010**, *75* (7), 2302−2308.

(38) Maes, J.; Rauws, T. R. M.; Maes, B. U. W. Synthesis of C8-N9 Annulated Purines by Iron-Catalyzed C-H Amination. *Chem. - Eur. J.* **2013**, *19* (28), 9137−9141.

(39) Sheikhi-Mohammareh, S.; Shiri, A.; Bakavoli, M. Synthesis of New Derivatives of Pyrazolo [4, 3-e][1, 2, 4] Triazolo [4, 3-c] Pyrimidine. *J. Chem. Res.* **2015**, *39* (7), 403−406.

(40) Sheikhi-Mohammareh, S.; Shiri, A.; Maleki, E. H.; Matin, M. M.; Beyzaei, H.; Baranipour, P.; Oroojalian, F.; Memariani, T. Synthesis of Various Derivatives of [1, 3] Selenazolo [4, 5-d] Pyrimidine and Exploitation of These Heterocyclic Systems as Antibacterial, Antifungal, and Anticancer Agents. *ChemistrySelect* **2020**, *5* (32), 10060−10066.

(41) Sheikhi-Mohammareh, S.; Shiri, A. An Alternative Regioselective Approach for the Synthesis of Highly Functionalized Derivatives of Pyrazolo [5, 1-b] Purine Scaffold. *J. Heterocycl. Chem.* **2018**, *55* (9), 2055−2060.

(42) Sheikhi-Mohammareh, S.; Shiri, A.; Mague, J. Dimroth Rearrangement-Based Synthesis of Novel Derivatives of [1,3]-Selenazolo[5,4-e][1,2,4]triazolo[1,5-c]pyrimidine as a New Class of Selenium-Containing Heterocyclic Architecture. *Mol. Diversity* **2021**, DOI: 10.1007/s11030-021-10203-9.

(43) Bigonah-Rasti, S.; Sheikhi-Mohammareh, S.; Saadat, K.; Shiri, A. Novel Tricyclic 2-Alkoxy-8-Methyl-6-(Pyrrolidin-1-Yl)-4 H-[1, 2, 4] Triazolo [5, 1-f] Purine Derivatives: Synthesis and Characterization. *Polycycl. Aromat. Compd.* **2020**, *41* (2), 1−11.

(44) Karimian, A.; Eshghi, H.; Bakavoli, M.; Shiri, A. Synthesis of Pyrimido [4′, 5′: 2, 3][1, 4] Thiazepino [7, 6-b] Quinolines, Derivatives of a Novel Ring System. *Heterocycl. Commun.* **2014**, *20* (5), 275−279.

(45) Mantell, M. A.; Lasky, M. R.; Lee, M.; Remy, M.; Sanford, M. S. SNAr and C-H Amination of Electron Rich Arenes with Pyridine as a Nucleophile Using Photoredox Catalysis. *Org. Lett.* **2021**, *23* (13), 5213−5217.

(46) Bariwal, J.; Van der Eycken, E. C-N Bond Forming Cross-Coupling Reactions: An Overview. *Chem. Soc. Rev.* **2013**, *42* (24), 9283−9303.

(47) Bruening, F.; Lovelle, L. E. Highly Regioselective Organocatalytic SNAr Amination of 2, 4-Dichloropyrimidine and Related Heteroaryl Chlorides. *Eur. J. Org. Chem.* **2017**, *2017* (22), 3222−3228.

(48) Priego, E.-M.; von Frijtag Drabbe Kuenzel, J.; IJzerman, A. P.; Camarasa, M.-J.; Pérez-Pérez, M.-J. Pyrido [2, 1-f] Purine-2, 4-Dione Derivatives as a Novel Class of Highly Potent Human A3 Adenosine Receptor Antagonists. *J. Med. Chem.* **2002**, *45* (16), 3337−3344.

(49) Priego, E.; Pérez-Pérez, M.; von Frijtag Drabbe Kuenzel, J. K.; de Vries, H.; IJzerman, A. P.; Camarasa, M.; Martín-Santamaría, S. Selective Human Adenosine A3 Antagonists Based on Pyrido [2, 1-f] Purine-2, 4-diones: Novel Features of HA3 Antagonist Binding. *ChemMedChem. Chem. Enabling Drug Discovery* **2008**, *3* (1), 111−119.

(50) Gong, W.; Gao, P.; Li, G.; Mehdi, H.; Ning, G.; Yu, J. Construction of Fluorescence-Tunable Pyrido-Fused Benzimidazoles via Direct Intramolecular C-H Amination under Transition-Metal-Free Conditions. *RSC Adv.* **2014**, *4* (93), 51268−51271.

(51) Lee, J. Y.; Shim, J. Y.; Kim, H. K.; Ko, D.; Baik, M.-H.; Yoo, E. J. 3, 5-Diarylimidazo [1, 2-a] Pyridines as Color-Tunable Fluorophores. *J. Org. Chem.* **2017**, *82* (8), 4352−4361.

(52) Mohadeszadeh, M.; Rahimizadeh, M.; Eshghi, H.; Shiri, A.; Gholizadeh, M.; Shams, A. Synthesis and Spectral Characteristics of Novel Fluorescent Dyes Based on Pyrimido [4, 5-d][1, 2, 4] Triazolo [4, 3-a] Pyrimidine. *Helv. Chim. Acta* **2015**, *98* (4), 474−481.

(53) Mokaber-Esfahani, M.; Eshghi, H.; Shiri, A.; Akbarzadeh, M.; Mirzaei, M. Synthesis of [1, 2, 4] Triazolo [3, 4-b] Pteridines as a Novel Class of Heterocyclic Compounds. *J. Chem. Res.* **2015**, *39* (4), 216−219.

(54) Brogi, S.; Ramalho, T. C.; Kuca, K.; Medina-Franco, J. L.; Valko, M. In Silico Methods for Drug Design and Discovery. *Front. Chem.* **2020**, *8*, 612.

(55) Daina, A.; Michielin, O.; Zoete, V. SwissADME: A Free Web Tool to Evaluate Pharmacokinetics, Drug-Likeness and Medicinal Chemistry Friendliness of Small Molecules. *Sci. Rep.* **2017**, *7* (1), 42717.

(56) Isa, M. A.; Mustapha, A.; Qazi, S.; Raza, K.; Allamin, I. A.; Ibrahim, M. M.; Mohammed, M. M. In Silico Molecular Docking and Molecular Dynamic Simulation of Potential Inhibitors of 3C-like Main Proteinase (3CLpro) from Severe Acute Respiratory Syndrome Coronavirus-2 (SARS-CoV-2) Using Selected African Medicinal Plants. *Adv. Tradit. Med.* **2020**, *53* (7), 1−17.

(57) Padilla-Salinas, R.; Sun, L.; Anderson, R.; Yang, X.; Zhang, S.; Chen, Z. J.; Yin, H. Discovery of Small-Molecule Cyclic GMP-AMP Synthase Inhibitors. *J. Org. Chem.* **2020**, *85* (3), 1579−1600.

(58) Kumar, D.; Kumari, K.; Vishvakarma, V. K.; Jayaraj, A.; Kumar, D.; Ramappa, V. K.; Patel, R.; Kumar, V.; Dass, S. K.; Chandra, R.; Singh, P. Promising Inhibitors of Main Protease of Novel Corona Virus to Prevent the Spread of COVID-19 Using Docking and Molecular Dynamics Simulation. *J. Biomol. Struct. Dyn.* **2021**, *39* (13), 4671−4685.

(59) Dolatkhah, Z.; Javanshir, S.; Sadr, A. S.; Hosseini, J.; Sardari, S. Synthesis, Molecular Docking, Molecular Dynamics Studies, and Biological Evaluation of 4 h-Chromone-1, 2, 3, 4-Tetrahydropyrimidine-5-Carboxylate Derivatives as Potential Antileukemic Agents. *J. Chem. Inf. Model.* **2017**, *57* (6), 1246−1257.

(60) Jin, Z.; Du, X.; Xu, Y.; Deng, Y.; Liu, M.; Zhao, Y.; Zhang, B.; Li, X.; Zhang, L.; Peng, C.; Duan, Y.; Yu, J.; Wang, L.; Yang, K.; Liu, F.; Jiang, R.; Yang, X.; You, T.; Liu, X.; Yang, X.; Bai, F.; Liu, H.; Liu, X.; Guddat, L. W.; Xu, W.; Xiao, G.; Qin, C.; Shi, Z.; Jiang, H.; Rao, Z.; Yang, H. Structure of Mpro from SARS-CoV-2 and Discovery of Its Inhibitors. *Nature* **2020**, *582* (7811), 289−293.

(61) Pettersen, E. F.; Goddard, T. D.; Huang, C. C.; Couch, G. S.; Greenblatt, D. M.; Meng, E. C.; Ferrin, T. E. UCSF Chimera—a Visualization System for Exploratory Research and Analysis. *J. Comput. Chem.* **2004**, *25* (13), 1605−1612.

(62) Xu, Y.; Wang, S.; Hu, Q.; Gao, S.; Ma, X.; Zhang, W.; Shen, Y.; Chen, F.; Lai, L.; Pei, J. CavityPlus: A Web Server for Protein Cavity Detection with Pharmacophore Modelling, Allosteric Site Identification and Covalent Ligand Binding Ability Prediction. *Nucleic Acids Res.* **2018**, *46* (W1), W374−W379.

(63) Frisch, M. J.; Trucks, G. W.; Schlegel, H. B.; Scuseria, G. E.; Robb, M. A.; Cheeseman, J. R.; Scalmani, G.; Barone, V.; Mennucci, B.;

Petersson, G. A.; Nakatsuji, H. *Gaussian 09*, rev. d.01; Gaussian, Inc.: Wallingford, CT, 2009.

(64) Abraham, M. J.; Murtola, T.; Schulz, R.; Páll, S.; Smith, J. C.; Hess, B.; Lindahl, E. GROMACS: High Performance Molecular Simulations through Multi-Level Parallelism from Laptops to Super-computers. *SoftwareX* **2015**, *1*, 19−25.

(65) Baker, N. A.; Sept, D.; Joseph, S.; Holst, M. J.; McCammon, J. A. Electrostatics of Nanosystems: Application to Microtubules and the Ribosome. *Proc. Natl. Acad. Sci. U. S. A.* **2001**, *98* (18), 10037−10041.

(66) Kumari, R.; Kumar, R.; Consortium, O. S. D. D.; Lynn, A. G_mmpbsa: A GROMACS Tool for High-Throughput MM-PBSA Calculations. *J. Chem. Inf. Model.* **2014**, *54* (7), 1951−1962.